

## THE REST-FRAME ULTRAVIOLET STRUCTURE OF $0.5 < Z < 1.5$ GALAXIES

NICHOLAS A. BOND, JONATHAN P. GARDNER<sup>1</sup>, DUILIA F. DE MELLO<sup>2</sup>, HARRY I. TEPLITZ, MARC RAFELSKI<sup>3</sup>, ANTON M. KOEKEMOER<sup>4</sup>, DAN COE<sup>4</sup>, NORMAN GROGIN<sup>4</sup>, ERIC GAWISER<sup>5</sup>, SWARA RAVINDRANATH<sup>6</sup>, CLAUDIA SCARLATA<sup>7</sup>

*Draft version September 21, 2021*

### ABSTRACT

We present the rest-frame UV wavelength dependence of the Petrosian-like half-light radius ( $r_{50}$ ), and the concentration parameter for a sample of 198 star-forming galaxies at  $0.5 < z < 1.5$ . We find a  $\sim 5\%$  decrease in  $r_{50}$  from 1500 Å to 3000 Å, with half-light radii at 3000 Å ranging from 0.6 kpc to 6 kpc. We also find a decrease in concentration of  $\sim 0.07$  ( $1.9 < C_{3000} < 3.9$ ). The lack of a strong relationship between  $r_{50}$  and wavelength is consistent with a model in which clumpy star formation is distributed over length scales comparable to the galaxy's rest-frame optical light. While the wavelength dependence of  $r_{50}$  is independent of size at all redshifts, concentration decreases more sharply in the far-UV ( $\sim 1500\text{Å}$ ) for large galaxies at  $z \sim 1$ . This decrease in concentration is caused by a flattening of the inner  $\sim 20\%$  of the light profile in disk-like galaxies, indicating that the central regions have different UV colors than the rest of the galaxy. We interpret this as a bulge component with older stellar populations and/or more dust. The size-dependent decrease in concentration is less dramatic at  $z \sim 2$ , suggesting that bulges are less dusty, younger, and/or less massive than the rest of the galaxy at higher redshifts.

*Subject headings:* cosmology: observations — galaxies: formation — galaxies: high-redshift — galaxies: structure

### 1. INTRODUCTION

Observations of galaxies at rest-frame ultraviolet wavelengths ( $\lambda \sim 1500$  Å) are important for tracing the evolution of star formation and dust obscuration. Until recently, the study of the structural properties of galaxies in the rest-frame ultraviolet has focused on  $z \gtrsim 2$ , as wavelengths  $< 3000$  Å and redward of the Lyman Break are easily accessible in the observed-frame optical using the Advanced Camera for Surveys (hereafter, ACS, Ford et al. 2003) on the *Hubble Space Telescope*<sup>8</sup>. Furthermore, the *Galaxy Evolution Explorer* (Martin et al. 2005) allows for the study of galaxy structure at  $z \lesssim 0.5$  (e.g., Kuchinski et al. 2000; Heckman et al. 2005; Taylor-Mager et al. 2007). With the installation of the Wide Field Camera 3 (hereafter, WFC3), including the UVIS channel, we now have the capability to directly observe the UV emission from hot stars in galaxies at  $0.5 < z < 1.5$ , a redshift interval that spans about one third of the history of the Universe.

Recently published studies of the morphological properties of  $0.5 < z < 1.5$  galaxies are drawn largely from the Cosmic Assembly Near-IR Deep Extragalactic Legacy Survey (CANDELS, Grogin et al. 2011; Koekemoer et al. 2011), which observed  $\sim 0.2$  deg<sup>2</sup> of sky in the optical and near-infrared with *HST*/ACS and *HST*/WFC3, respectively. In one such study, Wuyts et al. (2012) performed resolved spectral energy distribution (SED) fitting of 323 star-forming galaxies and found that the majority of recent star formation at  $0.5 < z < 1.5$  is occurring in clumps at or near the effective radius. These observations are consistent with theoretical models of gas-rich turbulent disks where clumps are supported by infalling cold streams of gas (Bournaud et al. 2007; Bournaud & Elmegreen 2009). There are alternative models involving mergers (e.g., Robertson & Bullock 2008), which may be important for a subset of galaxies at these redshifts, but fragmented structures in sources with clear rotation curves suggest that this is not the dominant mechanism (Genzel et al. 2008; Fruchter & Sosey 2009; Law et al. 2009; Shapiro et al. 2009).

At higher redshifts, rest-frame UV imaging with ACS reveals that most  $z > 2$  star-forming galaxies are clumpy, disturbed and disk-like in the rest-frame UV, with only  $\sim 30\%$  having light profiles consistent with galactic spheroids (e.g., Ferguson et al. 2004; Elmegreen & Elmegreen 2005; Lotz et al. 2006; Ravindranath et al. 2006; Petty et al. 2009). These studies find typical half-light radii of  $\sim 2$  kpc at  $z \sim 2 - 3$  and a size evolution that scales approximately as  $H^{-1}(z)$ . Although the UV wavelength dependence of galaxy structure has not been studied at high redshift, such studies have been carried out on well-resolved galaxies in the local universe. Taylor-Mager et al. (2007) found that morphology changes occur as one observes

<sup>1</sup> Cosmology Laboratory (Code 665), NASA Goddard Space Flight Center, Greenbelt, MD 20771

<sup>2</sup> Physics Department, The Catholic University of America, Washington, DC 20064 U.S.A.

<sup>3</sup> IPAC, California Institute of Technology, Pasadena, CA 91125

<sup>4</sup> Space Telescope Science Institute, 3700 San Martin Drive, Baltimore, MD 21218, U.S.A.

<sup>5</sup> Department of Physics and Astronomy, Rutgers University, Piscataway, NJ 08854

<sup>6</sup> Inter-University Centre for Astronomy and Astrophysics, Pune, India

<sup>7</sup> Minnesota Institute for Astrophysics, School of Physics and Astronomy, University of Minnesota, Minneapolis, MN 55455

<sup>8</sup> Based on observations made with the NASA/ESA Hubble Space Telescope, obtained [from the Data Archive] at the Space Telescope Science Institute, which is operated by the Association of Universities for Research in Astronomy, Inc., under NASA contract NAS 5-26555. These observations are associated with program number HST-GO-12534.

bluer in the UV, with galaxies becoming less concentrated, clumpier and more asymmetric.

We can obtain a clearer picture of the young stars in galaxies at  $0.5 \lesssim z \lesssim 1.5$  by studying their rest-frame UV emission at  $\lambda \sim 1000 - 4000 \text{ \AA}$ . Previous studies of star-forming galaxies in this redshift range were performed without the aid of observed-frame UV imaging (e.g., Bruce et al. 2012; Wuyts et al. 2012, 2013) or with relatively shallow imaging in a single filter (Voyer 2011; Rutkowski et al. 2012). In this paper, we use data taken as part of a program (GO 11563: PI Teplitz) to obtain UV imaging of the Hubble Ultra Deep Field (hereafter, UVUDF Teplitz et al. 2013) and study intermediate-redshift galaxy structure in the F336W, F275W, and F225W filters, complementing existing optical and near-IR measurements from the 2012 Hubble Ultra Deep Field (HUDF12, Ellis et al. 2013) survey. We use AB magnitudes throughout and assume a concordance cosmology with  $H_0 = 71 \text{ km s}^{-1} \text{ Mpc}^{-1}$ ,  $\Omega_m = 0.27$ , and  $\Omega_\Lambda = 0.73$  (Spergel et al. 2007). With these values,  $1'' = 8.0$  physical kpc at  $z = 1$ .

## 2. DATA AND METHODOLOGY

The UVUDF data and the optical Hubble Ultradeep Field (UDF, Beckwith et al. 2006) are both contained within a single deep field in the Great Observatories Origins Deep Survey South. The new UVUDF data include imaging in three filters (F336W, F275W, and F225W), obtained in ten visits, for a total of 30 orbits per filter. In addition, from the UDF, we make use of deep drizzled images taken in the observed optical with the F435W, F606W, and F775W filters. What follows is a brief summary of the observation strategy, data reduction, and catalog generation. For much greater detail on these procedures, see Teplitz et al. (2013, UVUDF), Beckwith et al. (2006, UDF), and (Rafelski et al, in prep).

The first half of the UVUDF observations were taken with  $2 \times 2$  onboard binning and without any artificial background added to the exposures. In the second half, in order to mitigate the effects of charge transfer inefficiency (CTI), the observations were done without binning and with an artificial ‘‘post-flash’’. We use only the second half of the observations for the following analysis. Although the effects of the CTI are mitigated by the post-flash, it could potentially still alter the apparent sizes of galaxies. We discuss and test this possibility in Section 2.3.

We reduced and calibrated the individual exposures incorporating overall bias frames, custom CTI-corrected dark frames and hot pixel removal (to be described in Rafelski et al., in prep), flat-fielding, and background subtraction that includes the removal of the post-flash. After applying a CTI correction to the raw data (using v1.0 of the standard CTI correction tool<sup>9</sup>), we combined the exposures using MultiDrizzle (Koekemoer et al. 2002), with a pixfrac of 0.8 and a square kernel, to produce final drizzled images with a pixel scale of 30 mas. Details of the image combination are the same as those described in Koekemoer et al. (2011). In order to ensure accurate alignment of the UV imaging with the UDF (Beckwith et al. 2006), the WFC3

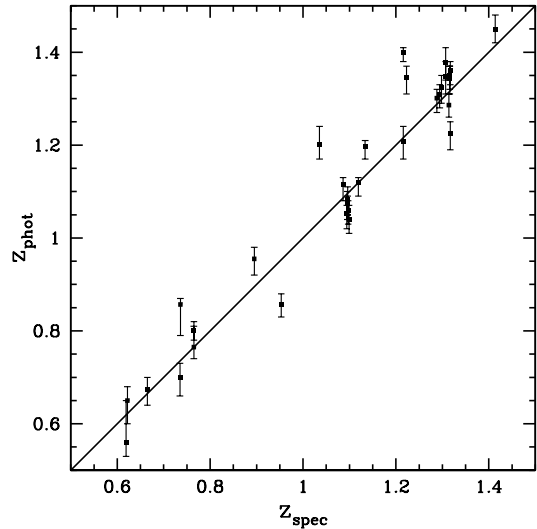


FIG. 1.— The photometric redshift plotted against the spectroscopic redshift for 33 galaxies in the UVUDF. The photometric redshifts have a scatter in  $\Delta z/(1+z)$  of  $\sigma_z = 0.030$ , after excluding one  $3\text{-}\sigma$  outlier, and the mean has a bias of  $\Delta z/(1+z) = 0.008 \pm 0.006$ .

exposures were individually aligned to the UDF B-band catalog.

We construct a source catalog (Rafelski et al, in prep), following a procedure similar to the Ultradeep Field catalog (Coe et al. 2006). All objects are detected using SExtractor (Bertin & Arnouts 1996) on an image that is the weighted sum of the F435W, F606W, F775W, F850LP ACS images and F105W, F125W, F140W, and F160W WFC3/IR images. This detection image is used to derive aperture corrections, which are then applied to isophotal magnitudes measured in the UV images. The effective depth; that is, the limiting magnitude at which sources have a  $> 50\%$  detection efficiency, is  $m_{\text{AB}} = 27.7, 27.7, 28.2$  for F225W, F275W, and F336W, respectively.

For all individual galaxies, we determined redshifts using a Bayesian photo- $z$  (BPZ) algorithm (Benítez 2000; Benítez et al. 2004; Coe et al. 2006), but the UVUDF catalog also includes spectroscopic redshifts, compiled by Rafelski et al. (2009) from a range of sources (Le Fèvre et al. 2004; Szokoly et al. 2004; Vanzella et al. 2005, 2006, 2008; Popesso et al. 2009). We also include new measurements from Balestra et al. (2010) and Kurk et al. (2013), giving a total of 33  $0.5 < z < 1.5$  galaxies with spectroscopic redshifts. We demonstrate the accuracy of the photometric redshifts in Figure 1 by comparing them to spectroscopic redshifts for these galaxies. The photometric redshifts have a scatter in  $\Delta z/(1+z)$  of  $\sigma_z = 0.030$  over the range,  $0.5 < z < 1.5$ . In addition, there is a bias of  $(z_{\text{phot}} - z_{\text{spec}})/(1+z) = 0.008 \pm 0.006$ , which we find to be insignificant at  $< 2\sigma$  using 1000 bootstrap simulations. We also used 125 G141 grism redshifts from the 3D-HST project (van Dokkum et al. 2013), which agree very well with the other spectroscopic redshifts,  $\sigma_z = 0.0056$ . For all samples here, we assume a galaxy is at its spectroscopic redshift, if one is available. If not, it is given either a grism redshift or, if no other measurement is available, a photometric redshift.

<sup>9</sup> [http://www.stsci.edu/hst/wfc3/tools/cte\\_tools](http://www.stsci.edu/hst/wfc3/tools/cte_tools)

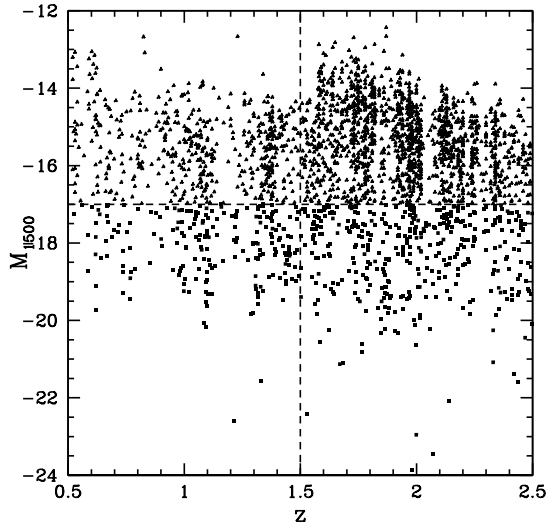


FIG. 2.— The distribution of absolute magnitude at 1500 Å as a function of redshift (see Section 2) for all sources in the UVUDF catalog. We separate our sample into two redshifts bins (vertical dashed line) and implement a cut at  $M_{1500} < -17$  (horizontal dashed line) to ensure a sample that is luminosity-limited in the UV and for which simple morphological diagnostics can be measured (average S/N per pixel  $\gtrsim 2$ ). Note that, at  $1.5 < z < 2.5$ , 1500 Å is sampled primarily by the deeper UDF optical imaging.

### 2.1. Sample Selection

We analyze two UV-luminosity-limited samples, one at  $0.5 < z < 1.5$  and another at  $1.5 < z < 2.5$ . We select each according to the rest-frame 1500 Å absolute magnitude,  $M_{1500}$ , which is estimated from a linear interpolation between the two nearest UV or optical magnitudes. In Figure 2, we show the distribution of  $M_{1500}$  as a function of redshift for galaxies in the UVUDF area. We implement a  $M_{1500} < -17$  cut to ensure completeness at all redshifts and sufficient signal-to-noise (S/N) that concentration measurements can be made in most bandpasses (S/N per pixel  $> 2$ , see Section 2.2 for more detail on the signal-to-noise requirements). Our source catalog is 100% complete for all galaxies brighter than this magnitude cut. The final luminosity-limited samples contain 198 galaxies at  $0.5 < z < 1.5$  and 400 galaxies at  $1.5 < z < 2.5$ .

### 2.2. Structural Diagnostics

We measure galaxy sizes with a Petrosian-like radius (Petrosian 1976); specifically, the radial distance at which the local surface brightness is half of the internal surface brightness,  $r_{50} \equiv r(\eta = 0.5)$ , and  $\eta(r) \equiv I(r)/\langle I(< r) \rangle$ . This quantity is approximately equal to the half-light radius. We define the concentration following Kent (1985) and Conselice (2003),

$$C = 5 \log \left[ \frac{r_{80\%}}{r_{20\%}} \right], \quad (1)$$

where  $(r_{80\%}, r_{20\%})$  are the radii at which the integrated light profile is at 80% and 20% of the light within  $r(\eta = 0.2)$ . Both quantities are defined in terms of a surface brightness ratio, so are insensitive to the depth of the imaging.

In order to access the rest-frame ultraviolet in  $0.5 < z < 1.5$  galaxies, we use filters in the observed-frame

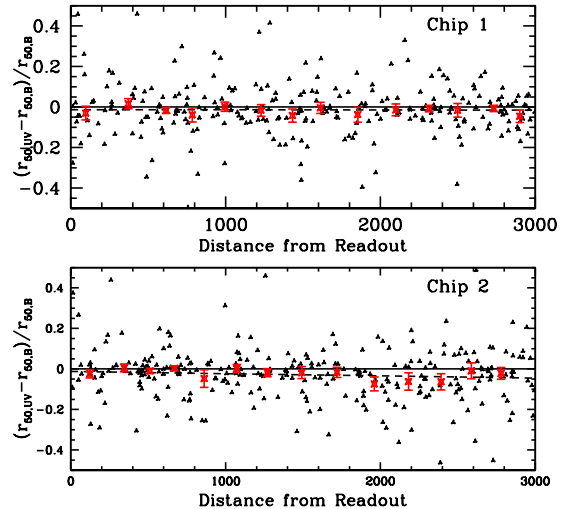


FIG. 3.— Fractional difference in  $r_{50}$  as a function of distance from the CCD readout for UVIS Chip 1 (top) and UVIS Chip 2 (bottom). Black triangles indicate individual galaxies, while red square points indicate the median differential radius in 10-object bins. Each panel includes a linear least squares fit (dashed line) to the data, both of which are consistent with the zero line (solid line) at  $< 1.5\sigma$ . If the CTI were having a significant impact on the  $r_{50}$  measurements, we would expect them to systematically decrease approaching the readout. No such effect is observed.

near-UV and optical, including F225W, F275W, and F336W from the UVUDF and F435W, F606W, and F775W from the UDF. All observed-frame UV structural measurements use the peak flux in the optical/near-IR detection image as the center of the galaxy (see Section 2). We checked that our results were insensitive to the filter used to center the galaxy, alternately using the F336W and B-band centroids as a reference position for the structural diagnostics. No qualitative change in our results is observed. Note that in order to achieve maximum spatial resolution, we do not match the point spread functions (PSFs) between the ACS and UVIS images. The PSF in the optical ACS images is  $\sim 10\%$  larger than that in the UVIS images, but most of the galaxies are well resolved and we show in Section 3 that such effects are not large enough to bias our results significantly.

In order to test the dependence of our structural diagnostics on S/N, we used object-by-object Monte Carlo simulations. To do this, we first extract the galaxies in our sample from the appropriate ACS image (nearest to  $\lambda_r = 3000$  Å) using SExtractor (DETECT\_MINAREA = 5 and DETECT\_THRESH = 1.65). The ACS images are much deeper than the corresponding WFC3 observations, and are therefore a good approximation of the galaxy’s “true” light distribution. We then simulated a noise-free WFC3 UVIS observation by normalizing this cutout so that the object’s aperture-corrected magnitude is the same as that in the real UV image. Noise was then added using actual realizations from blank regions in the epoch 3 WFC3 image. We find that there are systematic decreases in both  $r_e$  and  $C$  at very low S/N, but these decreases are  $< 1\%$  when the average S/N pixel is  $\gtrsim 2$  within a 1-pixel annulus centered at  $r(\eta = 0.5)$  and  $r_{80\%}$ , respectively. As such, we restrict our analyses in the UV to objects brighter than this limit.

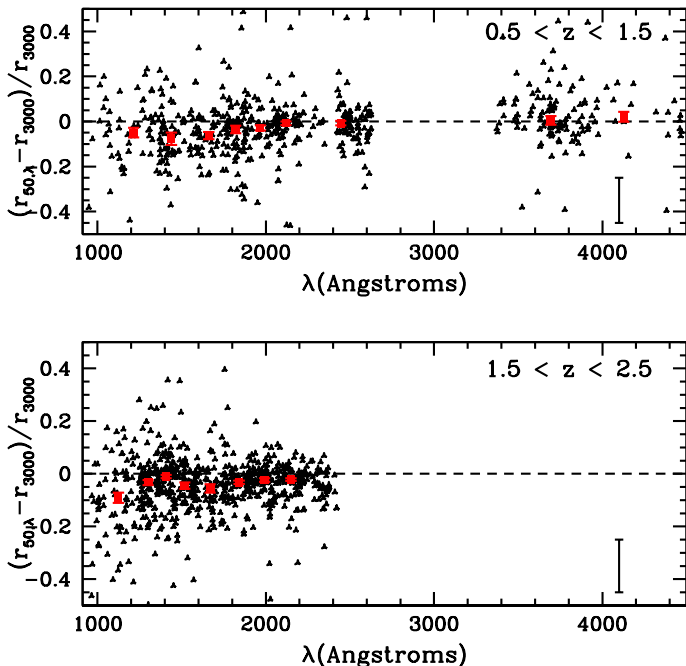


FIG. 4.— The difference in  $r_{50}$  as a function of rest-frame wavelength for a sample of 198  $0.5 < z < 1.5$  galaxies with  $M_{1500} < -17$  (top) and a sample of 400  $1.5 < z < 2.5$  galaxies with the same magnitude cutoff (bottom). Differences are taken relative to the filter nearest to rest-frame 3000 Å. Black triangles indicate individual measurements, while red square points indicate the median differential radius in 10-object bins. Error bars for the medians are derived from 1000 bootstrap simulations and a typical error bar for the individual measurements is given in the lower right corner. The median  $r_{50}$  exhibits a decrease at the bluest wavelengths, but remains constant to  $< 15\%$  over the range,  $1200 < \lambda_r < 4000$  Å.

### 2.3. Charge transfer inefficiency

One of the downsides to space-based CCD imaging is that the cumulative damage from cosmic radiation, in the form of charged particles, can create “charge traps” in the detector. When charge is transferred across the CCD in the readout phase, it can get caught in these traps, leading to a systematic loss of source flux in the processed image, as well as the creation of trails as the charge is eventually released later in the readout phase. This charge transfer inefficiency is especially problematic in UV images, where the sky background is low and the majority of the trapped charges will be from individually detected sources. In galaxies detected at moderate-to-high S/N, the CTI effects can be corrected, but sources at the faint end can be lost entirely due to these effects. The impact of CTI on galaxy shape measurements has been studied in the context of weak lensing (Rhodes et al. 2010), and it was found that galaxies far from the CCD readout can have their ellipticities altered by CTI effects.

For a detailed discussion of the impact of CTI on the UVUDF images and catalog, see Teplitz et al. (2013). In Figure 3, we plot the fractional difference in  $r_{50}$  as a function of distance from the CCD readout in the UVUDF observations. Each panel includes a linear least squares fit to the data (dashed line), both with slopes and y-intercepts that are consistent with zero at  $< 1.5\sigma$ . We

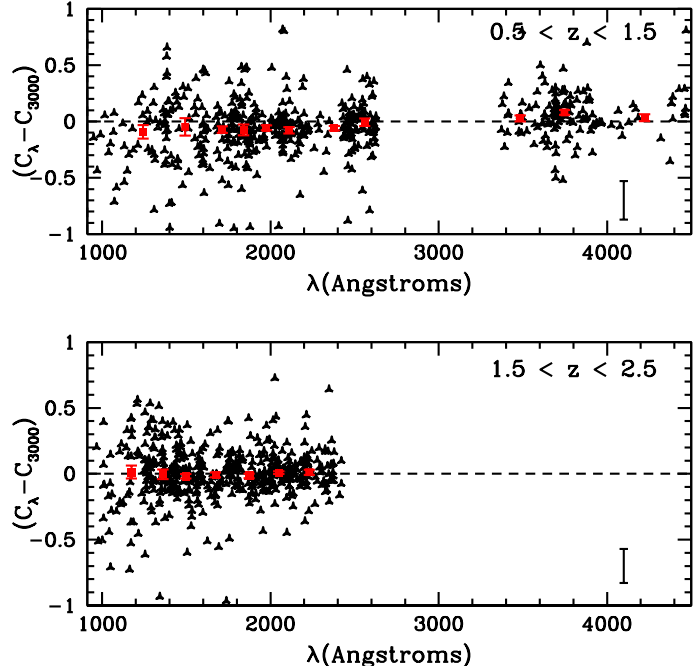


FIG. 5.— The same as Figure 4, except we plot the difference in concentration.

therefore infer that there is no systematic change in  $r_{50}$  as a function of distance from the readout, as one might expect if CTI effects were significant. Note that both the post-flash and the pixel-by-pixel CTI correction mitigate the effects of the CTI in these observations.

### 3. WAVELENGTH DEPENDENCE OF $r_{50}$ AND CONCENTRATION

Ultraviolet light in the rest frame of galaxies will be dominated by recent ( $\lesssim 100$  Myr) star formation, but observing bluer UV light allows us to distinguish the youngest ( $\sim 10$  Myr) star formation, as well as regions least extinguished by dust. By analyzing the wavelength dependence of simple structural diagnostics, such as  $r_{50}$  and concentration, we can characterize the spatial variation of these changes. In Table 1, we give the position, photometric redshift,  $M_{1500}$ ,  $r_{50}$  at 3000 Å ( $r_{3000}$ ), and  $C$  at 3000 Å ( $C_{3000}$ ) for each galaxy in the  $0.5 < z < 1.5$  sample.

In the top panel of Figure 4, we show how  $r_{50}$  depends upon rest-frame wavelength in our sample of  $0.5 < z < 1.5$  galaxies. For each galaxy, we plot the fractional difference in  $r_{50}$  relative to the filter nearest to rest-frame 3000 Å. This choice of wavelength ensures that the reference measurement is taken in the observed-frame optical UDF images, in which all of our galaxies are detected at high S/N. The reader should bear in mind that our observations use broadband filters, with typical widths at  $z \sim 1$  ranging from  $\Delta\lambda_r \sim 200$  Å at 1000 Å to  $\Delta\lambda_r \sim 1000$  Å at 4000 Å. Measurements near 912 Å, for example, will include light both blueward and redward of the Lyman Break.

As shown in Figure 4, the median  $r_{50}$  decreases at  $\lambda < 1800$  Å for galaxies in both redshift intervals. When we consider only points bluer than this wavelength, the

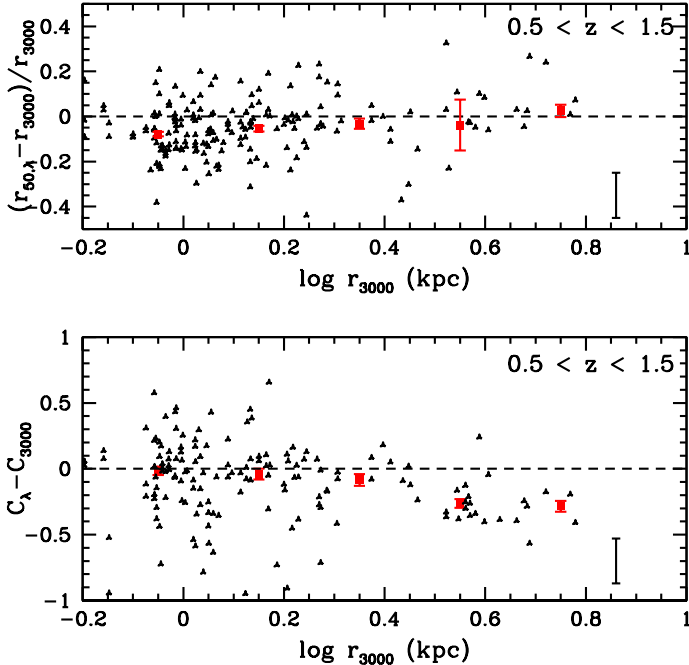


FIG. 6.— The difference in  $r_{50}$  (top panel) and concentration (bottom panel) as a function of  $r_{3000}$  for a sample of  $0.5 < z < 1.5$  galaxies with  $M_{1500} < -17$ . Differences are taken between far-UV wavelengths,  $\lambda_r < 1800 \text{ \AA}$ , and the filter nearest to rest-frame  $3000 \text{ \AA}$ . Black triangles indicate individual measurements, while red square points indicate the median differential radius in bins of  $\Delta \log r_{3000} = 0.2$ . Error bars for the medians are derived from 1000 bootstrap simulations and a typical error bar for the individual measurements is given in the lower right corner. The fractional difference in  $r_{50}$  is independent of size, while large galaxies are systematically less concentrated in the far-UV than the near-UV. This is likely due to the presence of bulges in many of the larger objects, which are faint at the bluest wavelengths.

median change in  $r_{50}$  is  $5.5\% \pm 0.9\%$ , while averaging over all  $\lambda < 3000 \text{ \AA}$  yields a change of  $3.0\% \pm 0.5\%$ . At  $z \sim 2$ , the same measurements give a decrease in  $r_{50}$  of  $3.7\% \pm 0.6\%$  and  $3.2\% \pm 0.3\%$ . The concentration, shown in Figure 5, also decreases at  $z \sim 1$  for  $\lambda < 1800 \text{ \AA}$ , with  $\Delta C = -0.07 \pm 0.02$  at  $z \sim 1$  ( $\Delta C = -0.06 \pm 0.01$  for  $\lambda < 3000 \text{ \AA}$ ). This is not consistent with the change in concentration seen at  $z \sim 2$  ( $\Delta C = -0.01 \pm 0.01$  for  $\lambda < 1800 \text{ \AA}$ ), suggesting that the wavelength dependence of concentration is more substantial at low redshift.

We also plot the fractional difference in  $r_{50}$  and concentration as a function of  $r_{3000}$  (see Figure 6) for all measurements at  $\lambda_r < 1800 \text{ \AA}$ . In addition to ensuring that the changes in morphology in the UVIS images are not due to the point spread function, this also helps us isolate the galaxies that are dominating the average trends shown in Figures 4 and 5. While the decrease of  $r_{50}$  in the FUV is approximately constant as a function of  $r_{3000}$ , concentration only decreases for galaxies with  $r_{3000} \gtrsim 2 \text{ kpc}$ . At  $z \sim 2$ , this effect is still present (Figure 7), but only for larger galaxies ( $r_{3000} \gtrsim 4 \text{ kpc}$ ).

To better understand the origin of the changes in concentration, we used the Kartaltepe et al. (2014) catalog to obtain  $H$ -band visual classifications for 111 galaxies in the  $0.5 < z < 1.5$  sample with  $H < 24.5$ , all with at least four reliable classifications. We define disk-like galaxies to

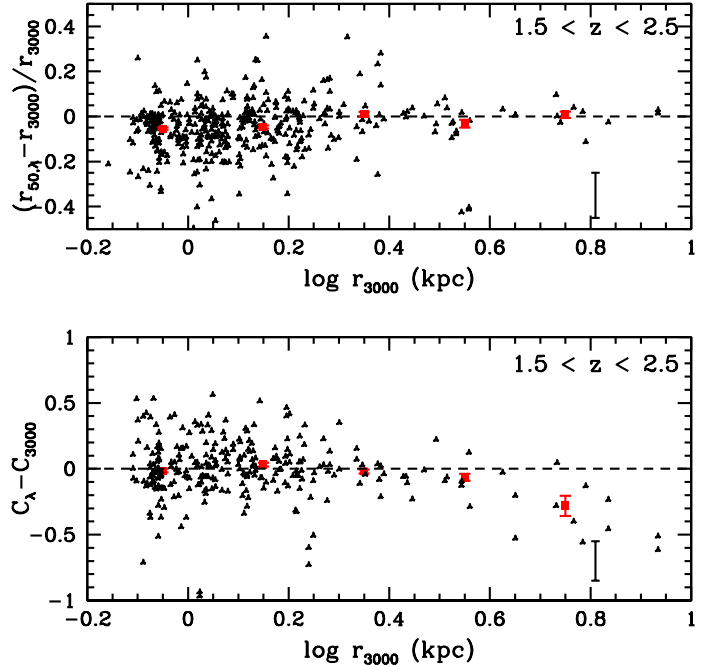


FIG. 7.— Same as Figure 6, but for the  $1.5 < z < 2.5$  sample. There is no evidence for a systematic decrease in concentration except for galaxies with  $r_{3000} \gtrsim 4 \text{ kpc}$ .

be those with sphericity  $> 0.5$ , where classifiers identified the galaxy as being disk-dominated. By contrast, spheroidal galaxies are those that were considered to be bulge-dominated in the rest-frame optical, or sphericity  $< 0.5$ . For spheroidal galaxies, the median change in concentration at  $\lambda < 1800 \text{ \AA}$  is consistent with zero, ( $C - C_{3000} = -0.02 \pm 0.03$ ), while disk-like galaxies exhibit a significant drop in concentration over the same wavelength range, with  $C - C_{3000} = -0.20 \pm 0.05$ . This result suggests that the decrease in concentration is occurring primarily in disk-like galaxies.

We can isolate the cause of this change even further by separately analyzing the wavelength dependence of  $r_{20\%}$  and  $r_{80\%}$  for the galaxies in our sample. Note that the difference in concentration between two wavelengths can be expressed as  $\Delta C$ , where

$$\Delta C = C_{\lambda_1} - C_{\lambda_2} = 5 \log \left[ \frac{r_{80\%,\lambda_1} r_{20\%,\lambda_2}}{r_{80\%,\lambda_2} r_{20\%,\lambda_1}} \right]. \quad (2)$$

A decrease in concentration in the FUV can occur due to a flattening of the inner part of the light profile,  $r_{20\%,1500} > r_{20\%,3000}$ , or a truncation of the wings,  $r_{80\%,1500} < r_{80\%,3000}$ , or some combination of both. In Figure 8, we show the difference of these parameters in the FUV as a function of  $r_{3000}$ . There is no evidence for a truncation of the outer light profile in the FUV for large galaxies. However, we do find evidence for an increase in the inner radius, with  $\Delta r_{20\%}/r_{20\%,3000} = 0.12 \pm 0.03$  for galaxies with  $r_{3000} > 2 \text{ kpc}$  compared to galaxies with  $r_{3000} < 2 \text{ kpc}$ . This suggests that the trend in Figure 6 is driven by a flattening of the central portion of the light profile, likely due to a decreasing contribution from the bulge of disk-like galaxies further in the FUV.

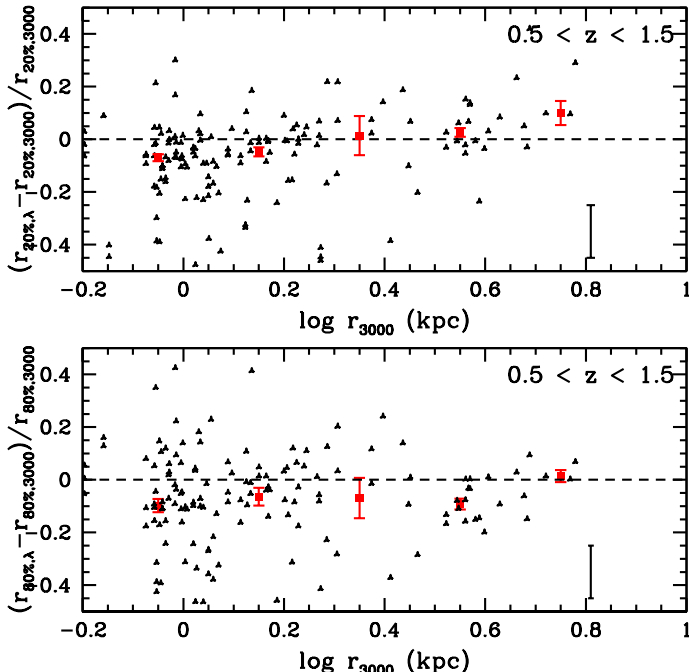


FIG. 8.— The difference in the 20% light radius (top panel) and the 80% light radius (bottom panel) as a function of  $r_{3000}$  for a sample of  $0.5 < z < 1.5$  galaxies with  $M_{1500} < -17$ . Data points are generated in the same way as in Figure 6 and a typical error bar for the individual measurements is given in the lower right corner. The fractional difference in the 20% light radius rises at large  $r_{3000}$ , suggesting that the central profiles of large galaxies are flattening in the far-UV. This is likely due to the presence of bulges or proto-bulges in many of the larger objects at  $z \sim 1$ .

#### 4. DISCUSSION

Previous studies of star-forming galaxies at  $0.5 < z < 1.5$  in the CANDELS survey (Wuyts et al. 2012) revealed that the youngest stellar populations at  $0.5 < z < 1.5$  tended to be concentrated in clumps near the effective radius (approximately equivalent to  $r_{50}$ ). In a simple 1 Gyr constant star formation model, they found that stars  $< 10$  Myr old will contribute  $\sim 60\%$  of the FUV light and stars  $< 100$  Myr old will contribute  $> 90\%$ . Therefore, we expect that young star-forming clumps, when present, will tend to set the physical scale on which both FUV and NUV emission are observed and  $r_{50}$  should be approximately constant across this rest-frame wavelength range.

However, far-UV observations of local Sa-Sb galaxies do reveal differences between the 3000 Å and 1500 Å

light profiles; in particular, they find that galaxies of type later than S0 exhibit a drop in concentration as one observes further into the FUV (Taylor-Mager et al. 2007). They attribute this change primarily to the diminished brightness of bulges at shorter wavelengths. Although the fraction of bulge-dominated galaxies decreases with redshift, we still expect  $\sim 60\%$  of our galaxies to be bulge-dominated at  $z \sim 1$  (Bruce et al. 2012).

Overall, our results are consistent with these expectations, although we do observe a small decrease in  $r_{50}$  ( $\sim 5\%$ ) in the FUV for samples at both  $0.5 < z < 1.5$  and  $1.5 < z < 2.5$ . The cause of this decrease is not clear, but it is independent of galaxy size. We also observe a decrease in concentration in the FUV, consistent with results at low redshift. It is only marginal for the sample as a whole ( $\Delta C \simeq 0.05$ , Figure 5), but the largest galaxies ( $r_{3000} > 2$  kpc) exhibit a drop of  $\Delta C \simeq -0.3$ , which we find to be due to a flattening of the central portion of the light profile for  $\lambda < 1800$  Å. A few illustrative examples are shown in Figure 9, where we plot the pixel-by-pixel color maps of four  $0.5 < z < 1.5$  galaxies between rest-frame 1500 Å and 3000 Å. We also show NIR cutouts from HUDF12 for comparison. While the majority of the UV emission is blue, with  $m_{1500} - m_{3000} \sim 0 - 1$ , the region near the rest-optical centroid tend to be redder than the rest of the galaxy. This is likely due to the presence of a bulge or proto-bulge near the center of the galaxy with older stellar populations and/or more dust than the rest of the galaxy.

To summarize, we find that a 1500 Å luminosity-limited sample of galaxies at  $0.5 < z < 1.5$  is both smaller ( $\sim 5\%$ ) and less concentrated ( $\Delta C \simeq 0.05$ ) at 1500 Å compared to 3000 Å. While the wavelength dependence of  $r_{50}$  is independent  $r_{3000}$  at all redshifts studied, the decrease in concentration is more substantial for galaxies with  $r \gtrsim 2$  kpc at  $z \sim 1$ . At  $z \sim 2$ , concentration is approximately constant across the rest-UV for all but the largest galaxies ( $r \gtrsim 4$  kpc). While we have painted a broad picture of the structural properties of star-forming galaxies in the FUV, a careful analysis of the spatial, size, and color distribution of star-forming clumps is underway (de Mello et al, in prep) and should provide us with a more detailed picture of the star formation in these galaxies.

Support for program number HST-GO-12534 was provided by NASA through a grant from the Space Telescope Science Institute, which is operated by the Association of Universities for Research in Astronomy, Inc., under NASA contract NAS 5-26555.

#### REFERENCES

- Balestra, I. et al. 2010, *A&A*, 512, A12+  
 Beckwith, S. V. W. et al. 2006, *AJ*, 132, 1729  
 Benítez, N. 2000, *ApJ*, 536, 571  
 Benítez, N. et al. 2004, *ApJS*, 150, 1  
 Bertin, E. & Arnouts, S. 1996, *A&AS*, 117, 393  
 Bournaud, F. & Elmegreen, B. G. 2009, *ApJ*, 694, L158  
 Bournaud, F., Elmegreen, B. G., & Elmegreen, D. M. 2007, *ApJ*, 670, 237  
 Bruce, V. A. et al. 2012, *MNRAS*, 427, 1666  
 Coe, D., Benítez, N., Sánchez, S. F., Jee, M., Bouwens, R., & Ford, H. 2006, *AJ*, 132, 926  
 Conselice, C. J. 2003, *ApJS*, 147, 1  
 Ellis, R. S. et al. 2013, *ApJ*, 763, L7  
 Elmegreen, B. G. & Elmegreen, D. M. 2005, *ApJ*, 627, 632  
 Ferguson, H. C. et al. 2004, *ApJ*, 600, L107  
 Ford, H. C. et al. 2003, in *Society of Photo-Optical Instrumentation Engineers (SPIE) Conference Series*, Vol. 4854, Future EUV/UV and Visible Space Astrophysics Missions and Instrumentation., ed. J. C. Blades & O. H. W. Siegmund, 81–94  
 Fruchter, A. S. & Sosey, M. 2009, version 3.0, (Baltimore, STScI)  
 Genzel, R. et al. 2008, *ApJ*, 687, 59  
 Grogin, N. A. et al. 2011, *ApJS*, 197, 35  
 Heckman, T. M. et al. 2005, *ApJ*, 619, L35  
 Kartaltepe, J. S. et al. 2014, *ArXiv e-prints*

- Kent, S. M. 1985, *ApJS*, 59, 115
- Koekemoer, A. M., Fruchter, A. S., Hook, R. N., & Hack, W. 2002, in *The 2002 HST Calibration Workshop : Hubble after the Installation of the ACS and the NICMOS Cooling System*, ed. S. Arribas, A. Koekemoer, & B. Whitmore, 337–+
- Koekemoer, A. M. et al. 2011, *ApJS*, 197, 36
- Kuchinski, L. E. et al. 2000, *ApJS*, 131, 441
- Kurk, J. et al. 2013, *A&A*, 549, A63
- Law, D. R., Steidel, C. C., Erb, D. K., Larkin, J. E., Pettini, M., Shapley, A. E., & Wright, S. A. 2009, *ApJ*, 697, 2057
- Le Fèvre, O. et al. 2004, *A&A*, 428, 1043
- Lotz, J. M., Madau, P., Giavalisco, M., Primack, J., & Ferguson, H. C. 2006, *ApJ*, 636, 592
- Martin, D. C. et al. 2005, *ApJ*, 619, L1
- Petrosian, V. 1976, *ApJ*, 209, L1
- Petty, S. M., de Mello, D. F., Gallagher, J. S., Gardner, J. P., Lotz, J. M., Matt Mountain, C., & Smith, L. J. 2009, *AJ*, 138, 362
- Popesso, P. et al. 2009, *A&A*, 494, 443
- Rafelski, M., Wolfe, A. M., Cooke, J., Chen, H., Armandroff, T. E., & Wirth, G. D. 2009, *ApJ*, 703, 2033
- Ravindranath, S. et al. 2006, *ApJ*, 652, 963
- Rhodes, J., Leauthaud, A., Stoughton, C., Massey, R., Dawson, K., Kolbe, W., & Roe, N. 2010, *PASP*, 122, 439
- Robertson, B. E. & Bullock, J. S. 2008, *ApJ*, 685, L27
- Rutkowski, M. J. et al. 2012, *ApJS*, 199, 4
- Shapiro, K. L. et al. 2009, in *Astronomical Society of the Pacific Conference Series*, Vol. 419, *Galaxy Evolution: Emerging Insights and Future Challenges*, ed. S. Jogee, I. Marinova, L. Hao, & G. A. Blanc, 60
- Spergel, D. N. et al. 2007, *ApJS*, 170, 377
- Szokoly, G. P. et al. 2004, *ApJS*, 155, 271
- Taylor-Mager, V. A., Conselice, C. J., Windhorst, R. A., & Jansen, R. A. 2007, *ApJ*, 659, 162
- Teplitz, H. I. et al. 2013, *ArXiv:astro-ph/1305.1357*
- van Dokkum, P. et al. 2013, *ArXiv:astro-ph/1305.2140*
- Vanzella, E. et al. 2005, *A&A*, 434, 53
- . 2006, *A&A*, 454, 423
- . 2008, *A&A*, 478, 83
- Voyer, E. N. 2011, PhD thesis, The Catholic University of America
- Wuyts, S. et al. 2012, *ApJ*, 753, 114
- . 2013, *ApJ*, 779, 135

TABLE 1  
GALAXY SAMPLES

Number	$\alpha$	$\delta$	$z$	$M_{1500}$	$r_{3000}$ (")	$C_{3000}$
1267	3:32:38.522	-27:48:38.327	1.341	-17.05 $\pm$ 0.12	0.119 $\pm$ 0.005	2.22 $\pm$ 0.08
1269	3:32:38.608	-27:48:37.577	1.425	-17.90 $\pm$ 0.09	0.157 $\pm$ 0.007	2.50 $\pm$ 0.09
1478	3:32:38.397	-27:48:28.997	1.489	-18.20 $\pm$ 0.08	0.441 $\pm$ 0.016	2.55 $\pm$ 0.12
1481	3:32:39.982	-27:48:30.610	0.959	-17.10 $\pm$ 0.12	0.189 $\pm$ 0.007	2.56 $\pm$ 0.10
1531	3:32:37.751	-27:48:30.170	1.496	-17.20 $\pm$ 0.12	0.219 $\pm$ 0.019	3.00 $\pm$ 0.14
1626	3:32:38.352	-27:48:25.728	1.458	-18.30 $\pm$ 0.08	0.517 $\pm$ 0.019	2.01 $\pm$ 0.11
1668	3:32:40.482	-27:48:26.558	1.167	-18.47 $\pm$ 0.07	0.129 $\pm$ 0.003	2.67 $\pm$ 0.07
1693	3:32:37.877	-27:48:26.719	1.120	-17.01 $\pm$ 0.13	0.130 $\pm$ 0.006	2.67 $\pm$ 0.09
1752	3:32:40.923	-27:48:24.006	1.470	-18.81 $\pm$ 0.05	0.098 $\pm$ 0.002	3.82 $\pm$ 0.08
1829	3:32:40.927	-27:48:23.646	1.298	-18.36 $\pm$ 0.07	0.165 $\pm$ 0.004	2.73 $\pm$ 0.07
1960	3:32:35.964	-27:48:11.906	0.605	-17.07 $\pm$ 0.12	0.129 $\pm$ 0.001	3.76 $\pm$ 0.04
2322	3:32:39.111	-27:48:01.844	1.270	-18.27 $\pm$ 0.07	0.102 $\pm$ 0.003	2.49 $\pm$ 0.07
2333	3:32:36.853	-27:48:13.103	1.310	-17.32 $\pm$ 0.11	0.237 $\pm$ 0.011	2.39 $\pm$ 0.10
2461	3:32:41.587	-27:48:08.252	1.123	-17.18 $\pm$ 0.12	0.150 $\pm$ 0.008	3.04 $\pm$ 0.11
2763	3:32:36.613	-27:48:01.254	1.492	-18.64 $\pm$ 0.06	0.335 $\pm$ 0.009	3.03 $\pm$ 0.11
2934	3:32:37.696	-27:48:02.420	1.143	-17.37 $\pm$ 0.11	0.110 $\pm$ 0.004	2.45 $\pm$ 0.07
2998	3:32:36.287	-27:47:55.285	0.713	-17.73 $\pm$ 0.10	0.361 $\pm$ 0.005	2.33 $\pm$ 0.07
3031	3:32:36.387	-27:47:58.585	1.439	-18.97 $\pm$ 0.05	0.474 $\pm$ 0.015	2.55 $\pm$ 0.11
3123	3:32:42.948	-27:47:55.134	1.065	-18.08 $\pm$ 0.08	0.185 $\pm$ 0.004	2.95 $\pm$ 0.08
3180	3:32:37.879	-27:47:51.079	0.768	-18.91 $\pm$ 0.05	0.336 $\pm$ 0.006	2.56 $\pm$ 0.10
3243	3:32:38.648	-27:47:56.206	1.355	-17.59 $\pm$ 0.11	0.367 $\pm$ 0.016	2.48 $\pm$ 0.12
3257	3:32:38.955	-27:47:55.095	1.379	-17.99 $\pm$ 0.09	0.501 $\pm$ 0.026	2.16 $\pm$ 0.12
3270	3:32:38.670	-27:47:55.696	1.229	-17.86 $\pm$ 0.09	0.255 $\pm$ 0.011	3.07 $\pm$ 0.12
3349	3:32:41.675	-27:47:50.462	0.668	-17.29 $\pm$ 0.12	0.500 $\pm$ 0.008	2.63 $\pm$ 0.09
3372	3:32:42.247	-27:47:46.139	0.794	-18.69 $\pm$ 0.07	0.734 $\pm$ 0.004	2.68 $\pm$ 0.08
3373	3:32:40.049	-27:47:51.790	0.995	-18.60 $\pm$ 0.07	0.449 $\pm$ 0.007	2.02 $\pm$ 0.08
3613	3:32:37.632	-27:47:44.300	1.097	-19.62 $\pm$ 0.02	0.410 $\pm$ 0.004	2.76 $\pm$ 0.07
3655	3:32:37.567	-27:47:50.181	1.327	-17.03 $\pm$ 0.12	0.110 $\pm$ 0.005	2.45 $\pm$ 0.08
3677	3:32:37.309	-27:47:29.362	0.669	-18.35 $\pm$ 0.07	0.270 $\pm$ 0.001	3.37 $\pm$ 0.06
3752	3:32:43.246	-27:47:44.003	1.440	-18.28 $\pm$ 0.07	0.154 $\pm$ 0.008	3.04 $\pm$ 0.10
3799	3:32:38.353	-27:47:44.418	1.442	-18.31 $\pm$ 0.08	0.710 $\pm$ 0.031	2.14 $\pm$ 0.13
3977	3:32:37.397	-27:47:41.601	1.095	-19.26 $\pm$ 0.04	0.555 $\pm$ 0.007	2.65 $\pm$ 0.08
4052	3:32:40.632	-27:47:39.997	1.040	-17.50 $\pm$ 0.11	0.240 $\pm$ 0.008	2.94 $\pm$ 0.11
4094	3:32:37.594	-27:47:39.531	0.663	-17.96 $\pm$ 0.09	0.136 $\pm$ 0.005	3.98 $\pm$ 0.12
4142	3:32:44.197	-27:47:33.527	0.737	-19.28 $\pm$ 0.03	0.240 $\pm$ 0.001	2.79 $\pm$ 0.02
4253	3:32:39.888	-27:47:38.261	1.049	-18.92 $\pm$ 0.05	0.459 $\pm$ 0.010	2.39 $\pm$ 0.10
4332	3:32:33.456	-27:47:39.512	1.403	-17.92 $\pm$ 0.09	0.131 $\pm$ 0.004	2.57 $\pm$ 0.07
4396	3:32:35.796	-27:47:34.736	1.223	-17.97 $\pm$ 0.09	0.145 $\pm$ 0.005	3.19 $\pm$ 0.10
4438	3:32:33.031	-27:47:30.633	0.977	-18.82 $\pm$ 0.06	0.700 $\pm$ 0.007	2.31 $\pm$ 0.09
4458	3:32:36.054	-27:47:37.796	1.340	-21.47 $\pm$ 0.06	0.132 $\pm$ 0.017	1.13 $\pm$ 0.13
4481	3:32:39.264	-27:47:36.704	1.367	-18.87 $\pm$ 0.05	0.187 $\pm$ 0.004	2.87 $\pm$ 0.07
4491	3:32:40.216	-27:47:32.979	1.095	-19.53 $\pm$ 0.03	0.578 $\pm$ 0.006	2.69 $\pm$ 0.08
4587	3:32:40.673	-27:47:30.997	0.667	-17.02 $\pm$ 0.13	0.266 $\pm$ 0.001	2.75 $\pm$ 0.04
4591	3:32:41.120	-27:47:34.595	1.009	-18.13 $\pm$ 0.08	0.410 $\pm$ 0.009	2.87 $\pm$ 0.10
4616	3:32:42.737	-27:47:33.986	1.427	-17.63 $\pm$ 0.11	0.435 $\pm$ 0.022	2.46 $\pm$ 0.13
4662	3:32:39.490	-27:47:34.663	1.098	-17.69 $\pm$ 0.10	0.221 $\pm$ 0.009	3.10 $\pm$ 0.11
4767	3:32:40.607	-27:47:30.247	0.669	-17.01 $\pm$ 0.15	1.384 $\pm$ 0.010	1.15 $\pm$ 0.09
4816	3:32:44.165	-27:47:29.447	1.220	-18.37 $\pm$ 0.07	0.198 $\pm$ 0.004	3.29 $\pm$ 0.09
4835	3:32:34.867	-27:47:30.689	1.317	-18.02 $\pm$ 0.08	0.188 $\pm$ 0.006	2.97 $\pm$ 0.10
4849	3:32:39.321	-27:47:32.174	1.379	-17.42 $\pm$ 0.11	0.165 $\pm$ 0.009	2.50 $\pm$ 0.10
4976	3:32:34.693	-27:47:28.019	1.466	-18.93 $\pm$ 0.05	0.186 $\pm$ 0.004	3.12 $\pm$ 0.10
4981	3:32:34.659	-27:47:28.019	1.438	-19.06 $\pm$ 0.04	0.157 $\pm$ 0.003	2.91 $\pm$ 0.08
4999	3:32:36.352	-27:47:27.985	1.378	-18.82 $\pm$ 0.05	0.215 $\pm$ 0.008	3.48 $\pm$ 0.11
5115	3:32:32.651	-27:47:27.333	1.355	-17.33 $\pm$ 0.11	0.136 $\pm$ 0.011	3.61 $\pm$ 0.13
5187	3:32:44.355	-27:47:23.776	0.953	-17.66 $\pm$ 0.10	0.163 $\pm$ 0.002	2.77 $\pm$ 0.06
5190	3:32:34.808	-27:47:21.839	1.316	-19.59 $\pm$ 0.03	0.443 $\pm$ 0.005	2.49 $\pm$ 0.08
5216	3:32:34.261	-27:47:24.090	1.098	-18.16 $\pm$ 0.09	0.570 $\pm$ 0.018	1.73 $\pm$ 0.11
5268	3:32:40.324	-27:47:22.809	0.619	-17.85 $\pm$ 0.10	0.336 $\pm$ 0.003	2.26 $\pm$ 0.06
5388	3:32:41.857	-27:47:21.901	1.325	-18.32 $\pm$ 0.08	0.368 $\pm$ 0.010	2.76 $\pm$ 0.10
5417	3:32:39.881	-27:47:15.011	1.095	-20.17 $\pm$ 0.01	0.935 $\pm$ 0.005	2.02 $\pm$ 0.08
5497	3:32:37.763	-27:47:21.200	1.092	-17.28 $\pm$ 0.12	0.284 $\pm$ 0.011	2.31 $\pm$ 0.10
5569	3:32:35.328	-27:47:18.478	0.674	-17.47 $\pm$ 0.11	0.273 $\pm$ 0.003	2.76 $\pm$ 0.06
5658	3:32:41.766	-27:47:16.831	1.096	-18.74 $\pm$ 0.06	0.272 $\pm$ 0.007	3.78 $\pm$ 0.11
5661	3:32:31.776	-27:47:20.194	1.412	-17.55 $\pm$ 0.10	0.178 $\pm$ 0.009	2.37 $\pm$ 0.10
5694	3:32:43.475	-27:47:12.921	1.095	-19.01 $\pm$ 0.05	0.630 $\pm$ 0.012	2.55 $\pm$ 0.11
5709	3:32:35.667	-27:47:19.137	1.221	-17.28 $\pm$ 0.11	0.104 $\pm$ 0.005	2.49 $\pm$ 0.08
5753	3:32:32.328	-27:47:18.364	1.027	-17.17 $\pm$ 0.12	0.194 $\pm$ 0.010	3.06 $\pm$ 0.11
5896	3:32:36.958	-27:47:15.773	1.123	-17.59 $\pm$ 0.10	0.141 $\pm$ 0.004	3.08 $\pm$ 0.09
5898	3:32:31.397	-27:47:13.085	1.479	-18.26 $\pm$ 0.08	0.351 $\pm$ 0.014	3.06 $\pm$ 0.12
5922	3:32:31.568	-27:47:11.164	1.008	-18.10 $\pm$ 0.09	0.522 $\pm$ 0.017	2.60 $\pm$ 0.12
5959	3:32:39.381	-27:47:14.263	1.109	-18.43 $\pm$ 0.07	0.122 $\pm$ 0.002	2.42 $\pm$ 0.04
5975	3:32:41.692	-27:47:13.562	1.450	-18.58 $\pm$ 0.06	0.204 $\pm$ 0.006	2.71 $\pm$ 0.09
5989	3:32:38.633	-27:47:11.356	1.134	-18.59 $\pm$ 0.07	0.395 $\pm$ 0.007	2.44 $\pm$ 0.08
5995	3:32:42.662	-27:47:13.106	0.968	-17.99 $\pm$ 0.09	0.217 $\pm$ 0.005	2.71 $\pm$ 0.09
6022	3:32:35.310	-27:47:13.588	1.392	-18.30 $\pm$ 0.07	0.116 $\pm$ 0.002	2.73 $\pm$ 0.06



TABLE 1 — *Continued*

Number	$\alpha$	$\delta$	$z$	$M_{1500}$	$r_{3000}$ (")	$C_{3000}$
6027	3:32:39.637	-27:47:09.132	1.317	-17.07 $\pm$ 0.12	0.129 $\pm$ 0.004	3.93 $\pm$ 0.12
6079	3:32:33.458	-27:47:12.392	1.298	-18.02 $\pm$ 0.09	0.226 $\pm$ 0.006	2.84 $\pm$ 0.09
6107	3:32:39.838	-27:47:11.861	1.081	-17.49 $\pm$ 0.11	0.271 $\pm$ 0.012	2.36 $\pm$ 0.10
6118	3:32:43.498	-27:47:11.931	1.090	-17.86 $\pm$ 0.09	0.187 $\pm$ 0.007	2.28 $\pm$ 0.13
6153	3:32:34.941	-27:47:10.169	1.380	-17.18 $\pm$ 0.12	0.126 $\pm$ 0.009	2.41 $\pm$ 0.12
6187	3:32:37.480	-27:47:10.491	0.980	-17.16 $\pm$ 0.12	0.230 $\pm$ 0.011	2.54 $\pm$ 0.10
6196	3:32:38.513	-27:47:10.667	0.990	-17.73 $\pm$ 0.10	0.131 $\pm$ 0.003	2.56 $\pm$ 0.06
6235	3:32:34.907	-27:47:10.439	1.380	-17.63 $\pm$ 0.10	0.150 $\pm$ 0.011	2.68 $\pm$ 0.13
6583	3:32:36.447	-27:47:05.094	1.224	-17.33 $\pm$ 0.11	0.126 $\pm$ 0.006	2.46 $\pm$ 0.08
6627	3:32:35.384	-27:47:04.258	0.989	-17.46 $\pm$ 0.11	0.122 $\pm$ 0.004	2.51 $\pm$ 0.07
6645	3:32:33.176	-27:47:03.842	1.326	-18.18 $\pm$ 0.08	0.498 $\pm$ 0.017	2.21 $\pm$ 0.11
6673	3:32:34.767	-27:47:04.379	1.272	-17.08 $\pm$ 0.12	0.116 $\pm$ 0.006	2.39 $\pm$ 0.08
6710	3:32:46.235	-27:47:01.682	0.980	-17.64 $\pm$ 0.10	0.244 $\pm$ 0.009	3.57 $\pm$ 0.12
6754	3:32:31.292	-27:47:02.375	1.093	-17.82 $\pm$ 0.09	0.148 $\pm$ 0.004	2.92 $\pm$ 0.09
6782	3:32:32.506	-27:47:01.983	1.446	-17.81 $\pm$ 0.09	0.156 $\pm$ 0.006	2.38 $\pm$ 0.09
6785	3:32:45.966	-27:46:57.754	1.331	-19.24 $\pm$ 0.05	0.972 $\pm$ 0.013	2.38 $\pm$ 0.10
6821	3:32:42.774	-27:46:59.066	1.119	-19.30 $\pm$ 0.04	0.445 $\pm$ 0.004	2.12 $\pm$ 0.07
6846	3:32:44.298	-27:47:00.016	1.143	-17.78 $\pm$ 0.09	0.108 $\pm$ 0.003	2.86 $\pm$ 0.07
6853	3:32:36.435	-27:46:58.344	0.852	-18.51 $\pm$ 0.06	0.150 $\pm$ 0.002	2.87 $\pm$ 0.05
6862	3:32:41.422	-27:46:51.453	0.620	-17.49 $\pm$ 0.11	0.584 $\pm$ 0.004	2.56 $\pm$ 0.08
6886	3:32:43.497	-27:46:59.091	1.400	-18.23 $\pm$ 0.08	0.185 $\pm$ 0.006	3.20 $\pm$ 0.10
6894	3:32:31.132	-27:47:00.305	1.160	-17.00 $\pm$ 0.13	0.122 $\pm$ 0.005	2.52 $\pm$ 0.08
6922	3:32:36.178	-27:46:57.265	1.315	-17.72 $\pm$ 0.11	0.808 $\pm$ 0.040	2.86 $\pm$ 0.14
6933	3:32:33.429	-27:46:50.462	0.735	-18.21 $\pm$ 0.08	0.547 $\pm$ 0.006	2.41 $\pm$ 0.09
6939	3:32:46.068	-27:46:58.713	1.050	-17.39 $\pm$ 0.11	0.345 $\pm$ 0.011	2.03 $\pm$ 0.10
6949	3:32:44.239	-27:47:00.136	1.379	-17.25 $\pm$ 0.11	0.114 $\pm$ 0.007	2.53 $\pm$ 0.09
6953	3:32:36.668	-27:46:57.684	0.765	-17.48 $\pm$ 0.11	0.183 $\pm$ 0.004	2.51 $\pm$ 0.07
6957	3:32:35.063	-27:46:58.738	1.441	-18.44 $\pm$ 0.07	0.217 $\pm$ 0.005	2.36 $\pm$ 0.08
6974	3:32:37.954	-27:46:51.919	0.620	-19.10 $\pm$ 0.05	0.839 $\pm$ 0.004	2.11 $\pm$ 0.07
7036	3:32:45.681	-27:46:55.206	1.317	-19.30 $\pm$ 0.03	0.155 $\pm$ 0.003	3.30 $\pm$ 0.09
7067	3:32:32.443	-27:46:56.403	1.454	-18.33 $\pm$ 0.07	0.191 $\pm$ 0.005	2.87 $\pm$ 0.09
7071	3:32:36.442	-27:46:55.134	0.900	-17.90 $\pm$ 0.09	0.386 $\pm$ 0.006	2.74 $\pm$ 0.10
7081	3:32:38.958	-27:46:56.325	1.436	-18.54 $\pm$ 0.07	0.674 $\pm$ 0.013	1.61 $\pm$ 0.10
7112	3:32:39.815	-27:46:53.531	1.110	-18.57 $\pm$ 0.07	0.409 $\pm$ 0.005	1.64 $\pm$ 0.07
7131	3:32:32.459	-27:46:54.033	1.451	-18.22 $\pm$ 0.08	0.124 $\pm$ 0.002	2.80 $\pm$ 0.06
7136	3:32:38.990	-27:46:56.715	1.429	-17.65 $\pm$ 0.10	0.108 $\pm$ 0.005	2.33 $\pm$ 0.12
7193	3:32:33.429	-27:46:55.382	1.456	-17.32 $\pm$ 0.11	0.190 $\pm$ 0.015	2.52 $\pm$ 0.12
7269	3:32:41.890	-27:46:51.271	0.734	-17.58 $\pm$ 0.11	0.464 $\pm$ 0.009	3.29 $\pm$ 0.11
7290	3:32:36.928	-27:46:53.993	1.229	-17.17 $\pm$ 0.12	0.143 $\pm$ 0.008	2.46 $\pm$ 0.09
7370	3:32:32.712	-27:46:51.543	1.451	-18.09 $\pm$ 0.08	0.121 $\pm$ 0.003	2.65 $\pm$ 0.07
7394	3:32:38.990	-27:46:51.045	1.372	-17.75 $\pm$ 0.09	0.104 $\pm$ 0.003	2.40 $\pm$ 0.07
7398	3:32:42.319	-27:46:51.088	0.631	-17.15 $\pm$ 0.12	0.107 $\pm$ 0.002	2.59 $\pm$ 0.05
7452	3:32:44.189	-27:46:46.967	0.670	-17.02 $\pm$ 0.13	0.270 $\pm$ 0.006	2.83 $\pm$ 0.10
7556	3:32:40.781	-27:46:15.757	0.622	-19.72 $\pm$ 0.04	1.288 $\pm$ 0.007	2.50 $\pm$ 0.09
7559	3:32:38.100	-27:46:13.849	0.998	-19.07 $\pm$ 0.05	0.498 $\pm$ 0.004	2.12 $\pm$ 0.07
7647	3:32:41.425	-27:46:15.093	1.010	-17.17 $\pm$ 0.12	0.334 $\pm$ 0.016	3.18 $\pm$ 0.13
7664	3:32:36.954	-27:46:15.563	0.865	-17.76 $\pm$ 0.10	0.402 $\pm$ 0.009	3.02 $\pm$ 0.11
7678	3:32:38.986	-27:46:15.225	1.049	-17.84 $\pm$ 0.09	0.251 $\pm$ 0.006	2.90 $\pm$ 0.10
7705	3:32:37.563	-27:46:46.761	1.337	-18.28 $\pm$ 0.08	0.264 $\pm$ 0.012	2.80 $\pm$ 0.12
7725	3:32:35.078	-27:46:15.658	1.316	-19.40 $\pm$ 0.04	0.626 $\pm$ 0.009	2.17 $\pm$ 0.09
7756	3:32:33.926	-27:46:16.861	1.492	-17.79 $\pm$ 0.10	0.372 $\pm$ 0.016	2.72 $\pm$ 0.12
7786	3:32:37.065	-27:46:17.122	1.274	-18.44 $\pm$ 0.07	0.157 $\pm$ 0.002	3.46 $\pm$ 0.07
7889	3:32:44.274	-27:46:20.116	0.877	-17.23 $\pm$ 0.12	0.224 $\pm$ 0.008	3.19 $\pm$ 0.11
7959	3:32:34.758	-27:46:42.929	1.484	-17.37 $\pm$ 0.11	0.132 $\pm$ 0.006	2.67 $\pm$ 0.09
7974	3:32:37.728	-27:46:42.620	1.307	-19.10 $\pm$ 0.04	0.209 $\pm$ 0.003	2.76 $\pm$ 0.07
7995	3:32:42.253	-27:46:25.289	1.288	-19.82 $\pm$ 0.02	0.731 $\pm$ 0.008	1.71 $\pm$ 0.09
8051	3:32:37.425	-27:46:22.491	1.106	-17.85 $\pm$ 0.09	0.209 $\pm$ 0.006	2.89 $\pm$ 0.10
8125	3:32:41.514	-27:46:40.353	1.102	-19.32 $\pm$ 0.04	0.451 $\pm$ 0.006	2.78 $\pm$ 0.09
8242	3:32:34.954	-27:46:24.329	1.100	-17.33 $\pm$ 0.11	0.122 $\pm$ 0.004	2.34 $\pm$ 0.07
8255	3:32:34.627	-27:46:37.799	1.101	-17.35 $\pm$ 0.11	0.135 $\pm$ 0.004	2.92 $\pm$ 0.09
8257	3:32:38.596	-27:46:31.277	0.618	-18.29 $\pm$ 0.09	0.913 $\pm$ 0.005	2.44 $\pm$ 0.08
8270	3:32:43.971	-27:46:32.448	0.980	-18.73 $\pm$ 0.06	0.409 $\pm$ 0.006	2.51 $\pm$ 0.08
8275	3:32:36.451	-27:46:28.164	0.772	-18.76 $\pm$ 0.05	0.142 $\pm$ 0.002	2.51 $\pm$ 0.09
8314	3:32:36.661	-27:46:31.014	0.999	-17.81 $\pm$ 0.09	0.254 $\pm$ 0.005	3.19 $\pm$ 0.09
8316	3:32:38.300	-27:46:28.458	1.122	-18.65 $\pm$ 0.06	0.186 $\pm$ 0.010	3.27 $\pm$ 0.12
8372	3:32:35.619	-27:46:32.847	0.586	-17.78 $\pm$ 0.10	0.466 $\pm$ 0.004	2.93 $\pm$ 0.08
8374	3:32:35.391	-27:46:30.507	1.069	-17.06 $\pm$ 0.12	0.154 $\pm$ 0.008	2.52 $\pm$ 0.09
8392	3:32:34.186	-27:46:34.620	1.376	-17.36 $\pm$ 0.11	0.174 $\pm$ 0.007	2.53 $\pm$ 0.09
8461	3:32:44.618	-27:46:32.174	1.426	-19.46 $\pm$ 0.04	0.673 $\pm$ 0.009	1.83 $\pm$ 0.09
8501	3:32:44.747	-27:46:37.303	1.377	-17.01 $\pm$ 0.13	0.159 $\pm$ 0.010	2.43 $\pm$ 0.10
8551	3:32:36.403	-27:46:31.375	1.018	-19.27 $\pm$ 0.04	0.339 $\pm$ 0.005	2.85 $\pm$ 0.09
8585	3:32:35.485	-27:46:27.297	1.099	-19.64 $\pm$ 0.02	0.230 $\pm$ 0.002	3.39 $\pm$ 0.09
8597	3:32:41.860	-27:46:34.471	1.485	-17.08 $\pm$ 0.12	0.180 $\pm$ 0.014	2.31 $\pm$ 0.12
8653	3:32:39.220	-27:46:36.104	1.319	-18.40 $\pm$ 0.07	0.134 $\pm$ 0.003	2.58 $\pm$ 0.07
8680	3:32:35.465	-27:46:36.987	1.086	-18.40 $\pm$ 0.07	0.162 $\pm$ 0.002	2.59 $\pm$ 0.06
8693	3:32:44.358	-27:46:38.866	0.524	-17.23 $\pm$ 0.12	0.570 $\pm$ 0.008	3.99 $\pm$ 0.12

TABLE 1 — *Continued*

Number	$\alpha$	$\delta$	$z$	$M_{1500}$	$r_{3000}$ (")	$C_{3000}$
8744	3:32:35.192	-27:46:38.968	1.080	-17.44 ± 0.11	0.137 ± 0.004	2.34 ± 0.07
8749	3:32:34.857	-27:46:40.469	1.099	-17.75 ± 0.10	0.403 ± 0.005	2.04 ± 0.08
8765	3:32:36.562	-27:46:40.614	1.414	-18.89 ± 0.05	0.296 ± 0.006	2.37 ± 0.08
8776	3:32:36.589	-27:46:39.714	1.425	-18.08 ± 0.08	0.110 ± 0.004	2.59 ± 0.08
8801	3:32:41.510	-27:46:42.183	1.308	-18.00 ± 0.09	0.518 ± 0.021	2.54 ± 0.12
8810	3:32:37.266	-27:46:10.342	0.736	-18.75 ± 0.06	0.501 ± 0.003	2.09 ± 0.06
8872	3:32:43.038	-27:46:43.974	1.343	-17.19 ± 0.12	0.156 ± 0.016	2.96 ± 0.13
8930	3:32:37.500	-27:46:45.351	1.270	-17.67 ± 0.10	0.167 ± 0.013	2.82 ± 0.12
8941	3:32:37.644	-27:46:41.810	1.317	-17.14 ± 0.12	0.121 ± 0.006	2.43 ± 0.09
9018	3:32:35.296	-27:46:42.328	1.098	-18.96 ± 0.05	0.495 ± 0.007	2.18 ± 0.09
9090	3:32:39.350	-27:46:09.673	1.378	-17.85 ± 0.09	0.188 ± 0.013	1.82 ± 0.14
9125	3:32:39.915	-27:46:06.911	1.294	-19.82 ± 0.02	0.707 ± 0.009	2.06 ± 0.09
9183	3:32:38.446	-27:46:09.527	1.064	-18.65 ± 0.06	0.448 ± 0.009	2.33 ± 0.10
9244	3:32:38.760	-27:46:03.496	0.690	-17.85 ± 0.09	0.149 ± 0.002	2.72 ± 0.05
9253	3:32:42.813	-27:46:05.635	0.676	-19.62 ± 0.03	0.874 ± 0.003	2.65 ± 0.06
9264	3:32:37.192	-27:46:08.062	1.096	-17.82 ± 0.09	0.191 ± 0.002	3.53 ± 0.08
9273	3:32:40.162	-27:46:05.680	1.068	-17.79 ± 0.10	0.403 ± 0.021	2.07 ± 0.12
9332	3:32:43.120	-27:46:07.553	1.486	-18.99 ± 0.05	0.492 ± 0.010	2.93 ± 0.10
9341	3:32:38.365	-27:46:00.618	1.046	-18.40 ± 0.07	0.395 ± 0.008	2.35 ± 0.10
9348	3:32:36.871	-27:46:04.013	0.640	-17.27 ± 0.11	0.140 ± 0.004	3.63 ± 0.11
9402	3:32:35.056	-27:45:59.698	0.954	-18.69 ± 0.06	0.341 ± 0.007	2.92 ± 0.10
9437	3:32:35.806	-27:45:49.046	0.738	-18.61 ± 0.07	0.759 ± 0.007	2.48 ± 0.08
9444	3:32:37.298	-27:45:57.892	1.096	-17.10 ± 0.13	0.376 ± 0.008	2.67 ± 0.10
9455	3:32:41.334	-27:45:54.454	0.581	-18.69 ± 0.06	0.519 ± 0.005	2.90 ± 0.09
9474	3:32:39.467	-27:45:57.073	1.065	-17.93 ± 0.09	0.445 ± 0.010	1.75 ± 0.10
9532	3:32:36.330	-27:46:00.055	0.895	-17.33 ± 0.11	0.164 ± 0.003	3.01 ± 0.07
9649	3:32:40.198	-27:46:02.859	1.052	-17.21 ± 0.12	0.426 ± 0.018	2.64 ± 0.11
9672	3:32:37.851	-27:45:22.370	0.925	-17.09 ± 0.12	0.156 ± 0.006	3.16 ± 0.10
9712	3:32:37.887	-27:45:18.769	0.906	-18.07 ± 0.08	0.157 ± 0.002	2.64 ± 0.06
9759	3:32:38.330	-27:45:44.208	1.337	-19.23 ± 0.04	0.644 ± 0.014	2.06 ± 0.11
9765	3:32:36.328	-27:45:41.035	0.978	-17.48 ± 0.11	0.255 ± 0.007	2.37 ± 0.09
9783	3:32:37.349	-27:45:37.821	1.390	-17.16 ± 0.12	0.129 ± 0.008	2.97 ± 0.11
9837	3:32:36.676	-27:45:39.144	1.061	-17.22 ± 0.12	0.279 ± 0.011	3.04 ± 0.11
9868	3:32:39.322	-27:45:32.924	1.150	-17.02 ± 0.13	0.344 ± 0.011	2.01 ± 0.10
9962	3:32:37.496	-27:45:26.631	0.858	-17.20 ± 0.12	0.159 ± 0.003	2.74 ± 0.07
9974	3:32:38.093	-27:45:26.839	1.025	-17.62 ± 0.11	0.504 ± 0.015	2.50 ± 0.11
9980	3:32:37.268	-27:45:28.192	1.170	-17.24 ± 0.12	0.119 ± 0.006	2.36 ± 0.08
20037	3:32:38.245	-27:46:30.078	1.216	-17.92 ± 0.09	0.184 ± 0.004	2.56 ± 0.08
56612	3:32:36.405	-27:45:40.645	1.004	-18.92 ± 0.05	0.122 ± 0.001	2.39 ± 0.03
56720	3:32:35.772	-27:45:48.596	0.699	-17.65 ± 0.10	0.261 ± 0.004	2.82 ± 0.10
56815	3:32:36.197	-27:45:36.565	0.562	-17.01 ± 0.13	0.561 ± 0.005	3.20 ± 0.10
56986	3:32:30.420	-27:46:57.275	1.439	-18.80 ± 0.05	0.162 ± 0.003	2.68 ± 0.07
57344	3:32:47.279	-27:46:50.154	0.678	-17.08 ± 0.12	0.185 ± 0.003	2.52 ± 0.06
57390	3:32:30.949	-27:46:49.565	1.050	-17.30 ± 0.11	0.118 ± 0.008	2.39 ± 0.11
57616	3:32:34.909	-27:46:00.389	1.285	-17.99 ± 0.09	0.253 ± 0.011	2.98 ± 0.12
58728	3:32:32.741	-27:46:30.003	1.307	-18.86 ± 0.05	0.209 ± 0.003	2.44 ± 0.07
60189	3:32:38.153	-27:45:13.398	0.768	-18.13 ± 0.08	0.370 ± 0.004	3.16 ± 0.08

<sup>1</sup> Index in Coe et al. 2006<sup>2</sup> Position based on an optical+IR detection image (Rafelski et al., in prep.)<sup>3</sup> 1500 Å rest-frame absolute magnitude<sup>4</sup> Petrosian-like half-light radius at rest-frame 3000 Å<sup>5</sup> Concentration parameter at rest-frame 3000 Å

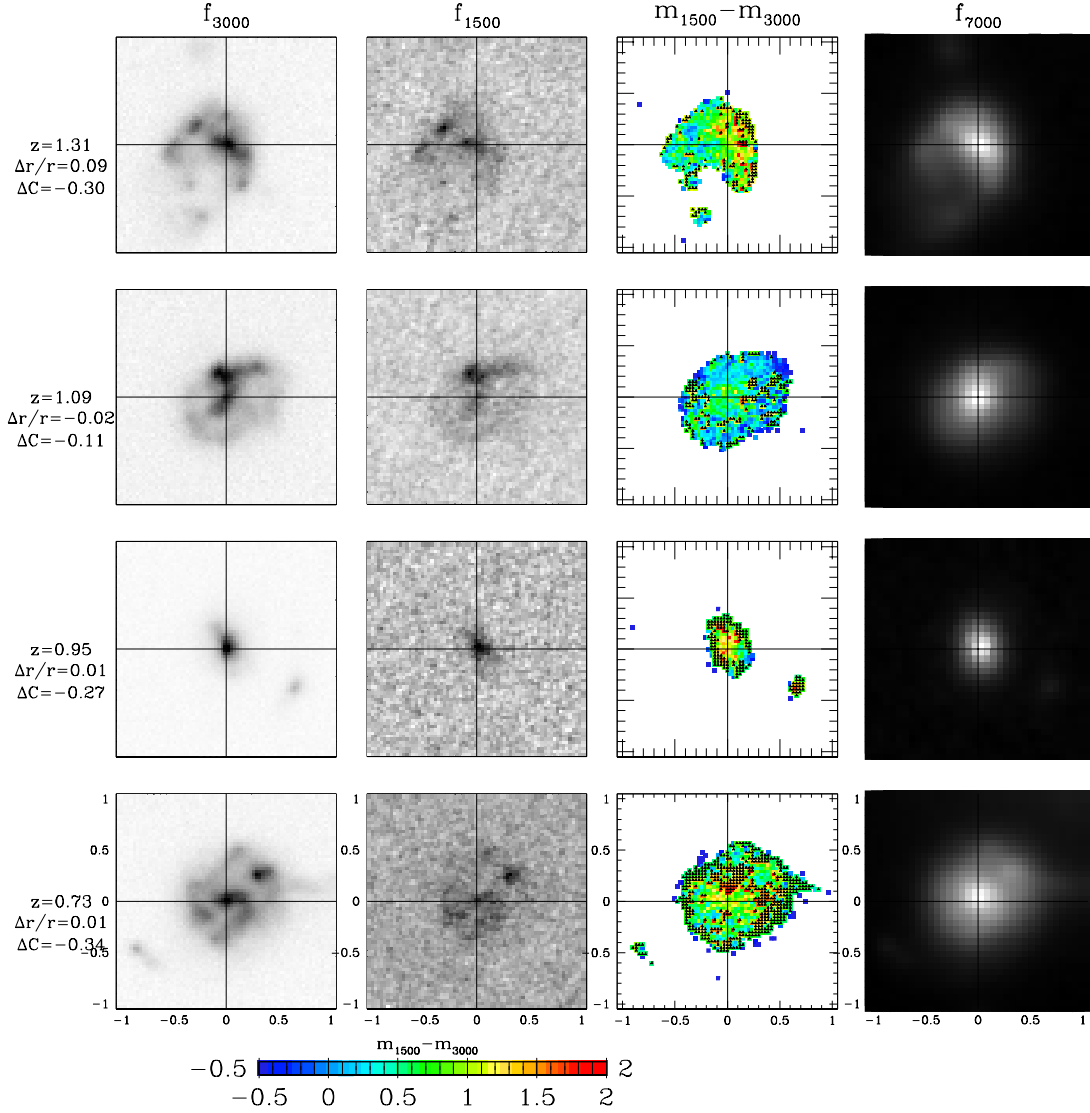


FIG. 9.— Panels demonstrating the change in morphology of  $0.5 < z < 1.5$  galaxies between rest-frame 1500 Å and 3000 Å. We show  $2''$  postage stamps of rest-frame 3000 Å (nearest UDF optical image), rest-frame 1500 Å (nearest UVIS image),  $m_{1500} - m_{3000}$ , and rest-frame 7000 Å (nearest HUDF12 image). The greyscale images are all scaled relative to the minimum and maximum in each panel and the colorscale is given at the bottom. When a pixel is not detected in the UVIS cutout, we color it with the  $1 - \sigma$  lower limit and overplot a small black triangle. To the left of each row, we give the galaxy redshift, difference in  $r_{50}$  between 1500 Å and 3000 Å, and difference in concentration between 1500 Å and 3000 Å.